frontiers | Frontiers in Physics

TYPE Original Research
PUBLISHED 29 August 2024
DOI 10.3389/fphy.2024.1440069

OPEN ACCESS

EDITED BY
Anna Palau,
Spanish National Research Council (CSIC), Spain

REVIEWED BY
Övgü Ceyda Yelgel,
Recep Tayyip Erdoğan University, Türkiye
Kapildeb Dolui,
University of Cambridge, United Kingdom

*CORRESPONDENCE
C. Trallero-Giner,
trallerocarlos@gmail.com

RECEIVED 28 May 2024
ACCEPTED 15 July 2024
PUBLISHED 29 August 2024

CITATION
Trallero-Giner C, Santiago-Pérez DG, Tkachenko DV, Marques GE and Fomin VM (2024), Transition metal dichalcogenides: magneto-polarons and resonant Raman scattering.
Front. Phys. 12:1440069.
doi: 10.3389/fphy.2024.1440069

Transition metal dichalcogenides: magneto-polarons and resonant Raman scattering

C. Trallero-Giner[1]*, D. G. Santiago-Pérez[2], D. V. Tkachenko[3], G. E. Marques[1] and V. M. Fomin[4,5]

[1]Departamento de Física, Universidade Federal de São Carlos, São Carlos, São Paulo, Brazil, [2]Departamento de Física, Centro de Investigación en Ciencias-IICBA, Universidad Autónoma del Estado de Morelos, Cuernavaca, Morelos, Mexico, [3]Department of Physics and Mathematics, Pridnestrovian State University, Tiraspol, Moldova, [4]Institute for Emerging Electronic Technologies (IET), Leibniz Institute for Solid State and Materials Research (IFW) Dresden, Dresden, Germany, [5]Faculty of Physics and Engineering, Moldova State University, Chişinău, Moldova

Topological two-dimensional transition metal dichalcogenides (TMDs) have a wide range of promising applications and are the subject of intense basic scientific research. Due to the existence of a direct optical bandgap, nano-optics and nano-optoelectronics employing monolayer TMDs are at the center of the development of next-generation devices. Magneto-resonant Raman scattering (MRRS) is a non-destructive fundamental technique that enables the study of magneto-electronic levels for TMD semiconductor device applications and hitherto unexplored optical transitions. Raman intensity in a Faraday backscattering configuration as a function of the magnetic field B, laser energy, and the circular polarization of light reveals a set of incoming and outgoing resonances with particular spin orientations and magneto-optical interband transitions at the K- and K'-valleys of the Brillouin zone. This fact unequivocally allows for a straightforward determination of the important band parameters of TMD materials. A generalization of the MRRS theory is performed for the description of the magneto-polaron (MP) effects in the first-order light scattering process. It shows how strongly the simultaneous presence of the conduction and valence bands modifies the MP energy spectrum. The resonant MP Raman intensity reveals three resonant splitting processes of double avoided-crossing levels reflecting the electron-hole pair energy spectrum. The scattering profile allows for quantifying the relative contribution of the conduction and valence bands in the formation of MPs. Many avoided-crossing points due to the electron–phonon interaction in the MP spectrum, a superposition of the electron and hole states in the excitation branches, and their impact on Raman scattering are exceptional features of monolayer TMDs. Based on this, the reported theoretical studies open a pathway toward MRRS and resonant MP Raman scattering characterization of two-dimensional materials.

KEYWORDS

Landau levels, magneto-polaron, Raman scattering, transition metal dichalcogenides, magneto-resonant Raman scattering

1 Introduction

Application of a magnetic field B leads to sharp features and strong oscillations in the first-order magneto-resonant Raman scattering (MRRS) intensity. The scattering efficiency is enhanced whenever an interband magneto-optical transition between Landau levels occurs [1]. Magneto-resonant spectroscopy is a very efficient tool for describing the electronic structure, determining the mixing effect of the valence bands, the electron-hole correlation, and for evaluating the band non-parabolicity in bulk semiconductors [2]. Furthermore, by employing different scattering configurations, MRRS allows for a manipulation of the intermediate electron–hole pair (EHP) states and their symmetry properties, while the relative intensities can be controlled by tuning the field. Two-dimensional (2D) materials in the presence of an external field B possess Dirac δ-singularities in the density of states, reinforcing the physical properties of the systems. MRRS is a powerful non-destructive tool used to study the total quantization of the EHP energy in 2D transition metal dichalcogenide (TMD) semiconductors [3]. By adjusting the laser energy and B, MRRS spectroscopy is a unique tool allowing one to analyze the fundamental differences between bulk systems and various 2D structures. The variations of the MRRS intensity with B open a promising road to novel efficient magneto-optical devices such as sensors and optical switches [4].

In a monolayer (ML) TMD, the optical phonon modes at the Γ-point of the Brillouin zone (BZ) belong to the symmetry group D_{3h} [5] with irreducible representations E', E'', A_1', and A_2'' [6]. The modes with E'(LO, TO) symmetry correspond to longitudinal LO and transverse TO in-plane oscillations, while the irreducible representation A'(ZO) is related to an out-of-plane ZO-phonon. The Raman tensors are written as [7].

$$E'\colon \begin{pmatrix} d_0 & d_1 & 0 \\ d_1 & -d_0 & 0 \\ 0 & 0 & 0 \end{pmatrix}; \qquad A_1'\colon \begin{pmatrix} f_0 & 0 & 0 \\ 0 & f_0 & 0 \\ 0 & 0 & g_0 \end{pmatrix}, \tag{1}$$

where d_0, d_1, f_0, and g_0 are the Raman polarizabilities.

We are searching the MRRS in 2D TMDs at the points K or K' of the Brillouin zone in the presence of the field B perpendicular to the plane (see Figure 1A). The first-order scattering process is a three-step process, represented in Figure 1B. First, the incoming light creates an EHP in the virtual state $|\mu_1\rangle$ with quantum numbers $(N_e, k_{ey}; N_h, k_{hy})$. Second, the EHP transition $|\mu_1\rangle = |N_e, k_{ey}; N_h, k_{hy}\rangle \rightarrow |\mu_2\rangle = |N_e', k_{ey}'; N_h', k_{hy}'\rangle$ takes place after the emission of an optical phonon ω_o by the electron or hole. Finally, the EHP is annihilated, emitting a photon of frequency ω_s. A quantitative picture of the scattering efficiencies allows us to delineate the key factors involved in the interband magneto-optical transitions between the conduction and valence bands at the K- or K'-points of the BZ, as well as to obtain valuable information about the fan plots of the Landau levels [2]. Having access to analytical models that can describe the MRRS in TMD materials becomes a necessity for understanding the Raman measurements. This allows for acquiring knowledge about the electron–phonon interaction and the band structure of the materials under study, as well as manipulating the Raman intensity through B and the laser energy.

At high magnetic fields, the Landau levels in the conduction or valence bands can be coupled by the energy of one optical phonon. This resonance effect is due to the electron–phonon interaction (EPI), lifting the degeneracy between two Landau levels separated by

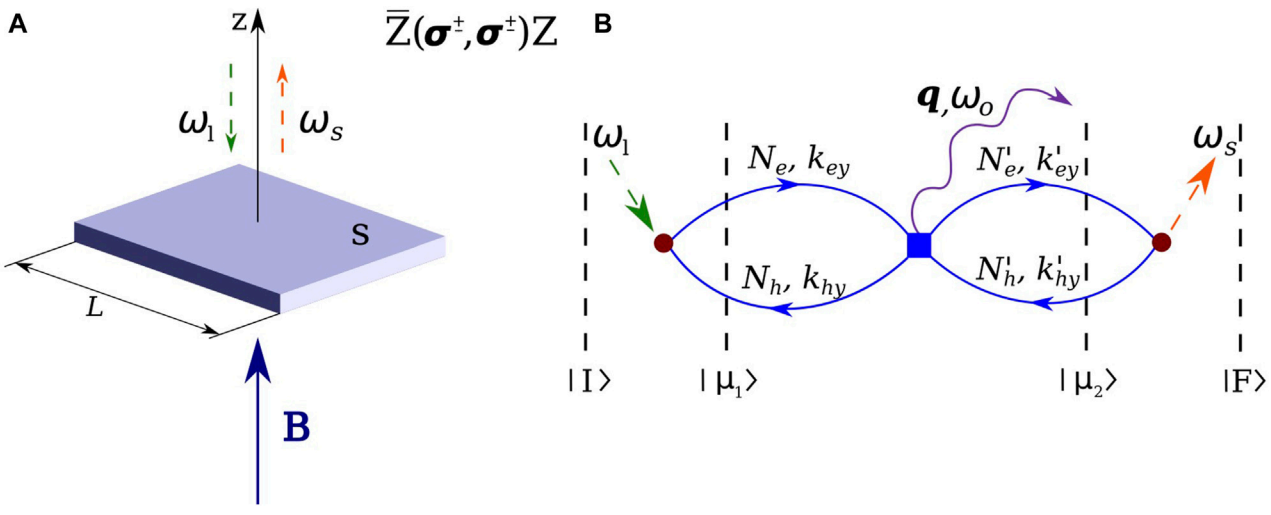

FIGURE 1
(A) Scheme of the magneto-Raman scattering measurement in a ML TMD in the Faraday backscattering configurations $\bar{Z}(\sigma^{\pm},\sigma^{\pm})Z$ with the magnetic field $\boldsymbol{B} \parallel \boldsymbol{e}_z$, $\sigma^{\pm} = \boldsymbol{e}_x \pm \boldsymbol{e}_y$ the polarization vector of the circularly polarized light, and ω_l (ω_s) the incident (scattered) photon frequency. **(B)** Resonant first-order scattering amplitude W_{FI}. Full circles and a square represent the electron–radiation and electron–phonon interactions, correspondingly, ω_o the optical phonon frequency with the phonon wave vector $\boldsymbol{q}$, $\mu = (N_e, k_{ey}; N_h, k_y)$ the virtual EHP states with the electron (hole) Landau level N_e (N_h) and the wave vector $\boldsymbol{k}_{ey}$ ($\boldsymbol{k}_{hy}$) along the y-direction.

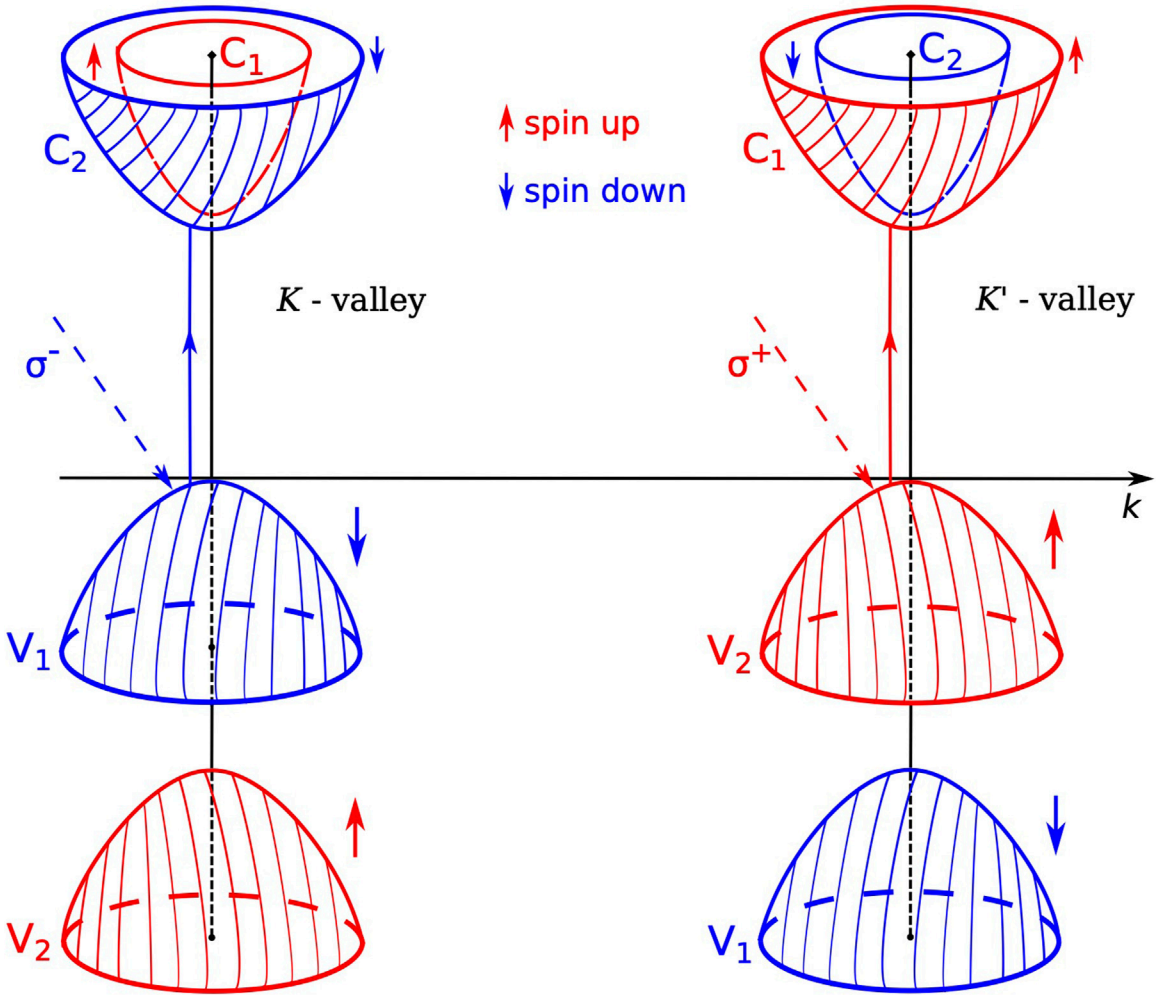

FIGURE 2
Scheme of the band structure of the ML MoX_2 family at the K- and K'-valleys. The conduction and valence sub-bands are denoted by C_i and V_i ($i = 1, 2$), respectively. The spin-up and spin-down orientations are symbolized by the red and blue arrows, and the allowed optical transitions, with the spin conservation, by the blue and red straight lines for σ^- and σ^+ light polarization, correspondingly.

an optical phonon; i.e., a resonant magneto-polaron (MP) coupling occurs. This effect was predicted in 1961 [8] and experimentally observed in the magneto-resistance of n-InSb [9]. MP effects have a huge impact on the transport properties [10], magneto-conductivity [11], cyclotron resonance [12], and magneto-optical properties [13]. Resonant magneto-polaron Raman scattering (RMPRS) measurements are useful to get accurate information on the band parameters in bulk semiconductors [14], phonon-impurity capture processes in Si [15], to describe the plasmon-LO–phonon interaction as a function of B [16], to study the quantum Hall effect and disorder in the graphene layers [17, 18]. A model describing RMPRS in III–IV bulk semiconductors was developed in [19, 20], where Raman intensities were reported for the scattering configurations, when an LO–phonon is emitted via intraband processes due to the Pekar-Fröhlich (PF) EPI or interband transitions owing to the deformation potential (DP) EPI. In the MP range, the intermediate EHP virtual states are renormalized by PF and DP interactions. MP resonances in graphene were addressed in the literature. The electronic states in a high field give rise to a series of discrete Landau levels, which couple to the E_{2g}-phonon [18, 21, 22].

This paper presents a rigorous description of RMPRS in an ML TMD on the basis of Green's function formalism. We find the peculiarities of the EHP MP spectrum that includes the coupling of the different Landau states for the electrons and holes with EPI in a systematic way. The MPRRS studies are required for characterizing TMD semiconductors [23] and for the study of disorder and doping in 2D materials [24, 25].

Our main objective is to describe the effects of a magnetic field on RRS in ML TMD semiconductors. For a better understanding and aiming at comparison of results, we split the study into processes with and without MP resonances. Section 2 describes general aspects of the first-order RSS in a magnetic field and magneto-Raman selection rules, and an explicit expression for the scattering efficiency via the A_1'-DP EPI is derived. Furthermore, an analysis of the incoming and outgoing resonances in different scattering configurations with circularly polarized light and its relationship to the symmetry of the band

TABLE 1 Parameters employed for the evaluation of the Raman intensity. $m_{e(c_1)}$ ($m_{e(c_2)}$) is the electron effective mass of the C1 (C2) conduction band, and $m_{h(v_1)}$ ($m_{h(v_2)}$) is the hole effective mass of the V1 (V2) valence band. a is the lattice constant, ω_{A_1} is the phonon frequency with the symmetry A_1', $g_e - g_h$ is the EH g-factor, $\alpha_{DP}^{(EH)}$ is the EH-phonon DP coupling constant, and E_g is the gap energy. m_0 is the free electron mass.

	MoS_2	$MoSe_2$	$MoTe_2$	WS_2	WSe_2
$m_{e(c_1)}/m_0$[a]	0.46	0.56	0.62	0.26	0.28
$m_{e(c_2)}/m_0$[a]	0.43	0.49	0.53	0.35	0.39
$m_{h(v_1)}/m_0$[a]	0.54	0.59	0.66	0.35	0.36
$m_{h(v_2)}/m_0$[a]	0.61	0.7	0.82	0.49	0.54
$\hbar\omega_{A_1}$ (meV)[b]	49.5	29.4	21.1	51	30.2
$g_e - g_h$	−4.2[c]	−4.2[c]	−4.6[d]	−4.0[e]	−3.8[c]
a (Å)[b]	3.1635	3.2974	—	3.1627	3.2954
$\alpha_{DP}^{(EH)}$	0.0323	0.0577	—	0.0070	0.0044
E_g (eV)[f]	1.85	1.59	1.22	1.99	1.74

[a][28].
[b][6].
[c][44].
[d][45].
[e][46].
[f][47].

parameters (effective masses and EH g-factors) of ML TX_2-family (T = Mo, W; X = S, Se, and Te) at the K- and K'-valleys are discussed. In Section 2.4, by employing Green's function formalism, a generalization of the results of Subsection 2.1 on RMPRS is performed including the MP effects on Raman scattering. Conclusion is listed in Section 3. The detailed calculations of Raman intensities and the procedure for obtaining the MP spectrum are summarized in the Supplementary Material.

2 One-phonon resonant Raman scattering in 2D TMD in a magnetic field

The differential Raman scattering cross-section $\partial^2\sigma/(\partial\Omega\partial\omega_s)$ per unit solid angle Ω and per unit scattered frequency ω_s is related to the scattering amplitude W_{FI} [26] from the initial state I of the system in the presence of an incident photon of frequency ω_l to the final state F for Stokes scattering by an optical phonon ω_o. It can be written as [27]

$$\frac{\partial^2\sigma}{\partial\Omega\partial\omega_s} \propto |W_{FI}|^2\delta(\hbar\omega_l - \hbar\omega_s - \hbar\omega_o). \quad (2)$$

In resonance, the main contribution of the first-order MRRS amplitude W_{FI} is represented by the Feynman diagram in Figure 1B; thus, it follows that

$$W_{FI} = \sum_{\mu_1\mu_2} \langle F|\hat{H}_{E-R}^{(+)}(\boldsymbol{\sigma}^{\pm})|\Psi_{\mu_2}\rangle G_{\mu_2}^{(0)}(\hbar\omega_l - \hbar\omega_o)\langle\Psi_{\mu_2}|\hat{H}_{E-P}|\Psi_{\mu_1}\rangle \times G_{\mu_1}^{(0)}(\hbar\omega_l)\langle\Psi_{\mu_1}|\hat{H}_{E-R}^{(-)}(\boldsymbol{\sigma}^{\pm})|I\rangle, \quad (3)$$

where $\hat{H}_{E-R}^{(\pm)}$ and $\hat{H}_{E-P}$ are the electron–radiation and electron–phonon Hamiltonians, respectively; the summation in Eq. 3 is carried over all virtual intermediate EHP states $|\Psi_{\mu_i}\rangle$ $(i = 1, 2)$ with energy ϵ_{μ_i}; $G_{\mu_i}^{(0)}(E) = [E - \epsilon_{\mu_i} + i\delta]^{-1}$ the EHP unperturbed Green's function at $T = 0$ K; and δ a residual lifetime broadening. The electron–radiation matrix element for the dipole-allowed magneto-optical transitions (detailed in Supplementary Material Section S1) is cast as

$$\langle\Psi_{\mu_1}|\hat{H}_{E-R}^{(-)}(\boldsymbol{\sigma}^{\pm})|I\rangle = \pm e\sqrt{\frac{4\pi}{\hbar\omega\eta^2}}\,\frac{at}{\sqrt{V}}\delta_{N_e,N_h}\delta_{k_{hy},k_{ey}-\kappa_y}\delta_{s_e,s_h}\boldsymbol{\sigma}\cdot\boldsymbol{\sigma}^{\mp}. \quad (4)$$

The same result is obtained for the $\langle F|\hat{H}_{E-R}^{(+)}(\boldsymbol{\sigma}^{\pm})|\Psi_{\mu_2}\rangle$. From Eq. 4, the conservation of spins $\Delta s = s_e - s_h = 0$ and Landau levels $\Delta N = N_e - N_h = 0$ follows. Figure 2 schematically represents the band structure in the vicinity of the K- and K'-valleys for a ML MoX_2 (X=S, Se, and Te). The conduction and valence bands are spin-split due to a strong spin–orbit coupling. The sub-bands are indicated by C_1, C_2 and V_1, and V_2 for the conduction and valence bands, respectively, while the spin orientation is symbolized by red and blue colors for spin-up and spin-down, respectively [28]. In the vicinity of the K (K')-valley, the optical transition is dipole allowed for the $\boldsymbol{\sigma}^-$ ($\boldsymbol{\sigma}^+$) polarization. Selection rules preserving the spin orientation for the $\boldsymbol{\sigma}^-$ and $\boldsymbol{\sigma}^+$ light polarization are illustrated in Figure 2 by vertical arrows between the valence and conduction bands. In case of the MoX_2 family, the $\boldsymbol{\sigma}^-$ polarization connects the $V_1 \rightarrow C_2$ bands at the K- or K'-points, while the $\boldsymbol{\sigma}^+$ polarization plugs $V_2 \rightarrow C_1$ bands. For the tungsten-based structures, the order of the spin orientation in the conduction band is reverse. Hence, for the $\boldsymbol{\sigma}^-$ ($\boldsymbol{\sigma}^+$) polarization, the interband optical transitions occur between the valence band V_1 (V_2) and the conduction band C_1 (C_2) at the K (K')-valley. In general, the light polarizations $\boldsymbol{\sigma}^{\pm}$ connect the $|V\rangle$ <–> $|C\rangle$ Bloch states with the change in the total angular momentum $\Delta J = \pm 1$ [29]. We assume that the laser excitation is well above the band gap ($\hbar\omega_l > E_g$), where the wave function of the EHP can be taken as that of the free particle. Under these conditions, the optical measurement is ruled by the Landau levels and the Zeeman splitting. If $\hbar\omega_l \approx E_g$, the diamagnetic shift for the excitons is observed in the magneto-optical spectra [30].

2.1 Scattering efficiency

In the Faraday backscattering configuration from the surface S of a ML at the parallel polarization $\bar{Z}(\boldsymbol{\sigma}_s^{\pm}, \boldsymbol{\sigma}_l^{\pm})Z$, as shown in Figure 1A, the components of the Raman tensors (Equation 1) allow two phonon modes with the symmetry E'(LO) and A_1'(ZO) via intra-valley EPI. For the in-plane longitudinal E'(LO) mode, the first-order Raman scattering is mediated by the long-range PF interaction, while for the out-of-plane ZO-branch, it occurs due to the short-range DP coupling.

2.2 Long-range interaction

In the backscattering configuration $\bar{Z}(\boldsymbol{\sigma}^{\pm}, \boldsymbol{\sigma}^{\pm})Z$, the in-plane phonon wave vector is 0. Hence, from Eqs 3, 4; Supplementary Equation S12, the scattering amplitude follows to be

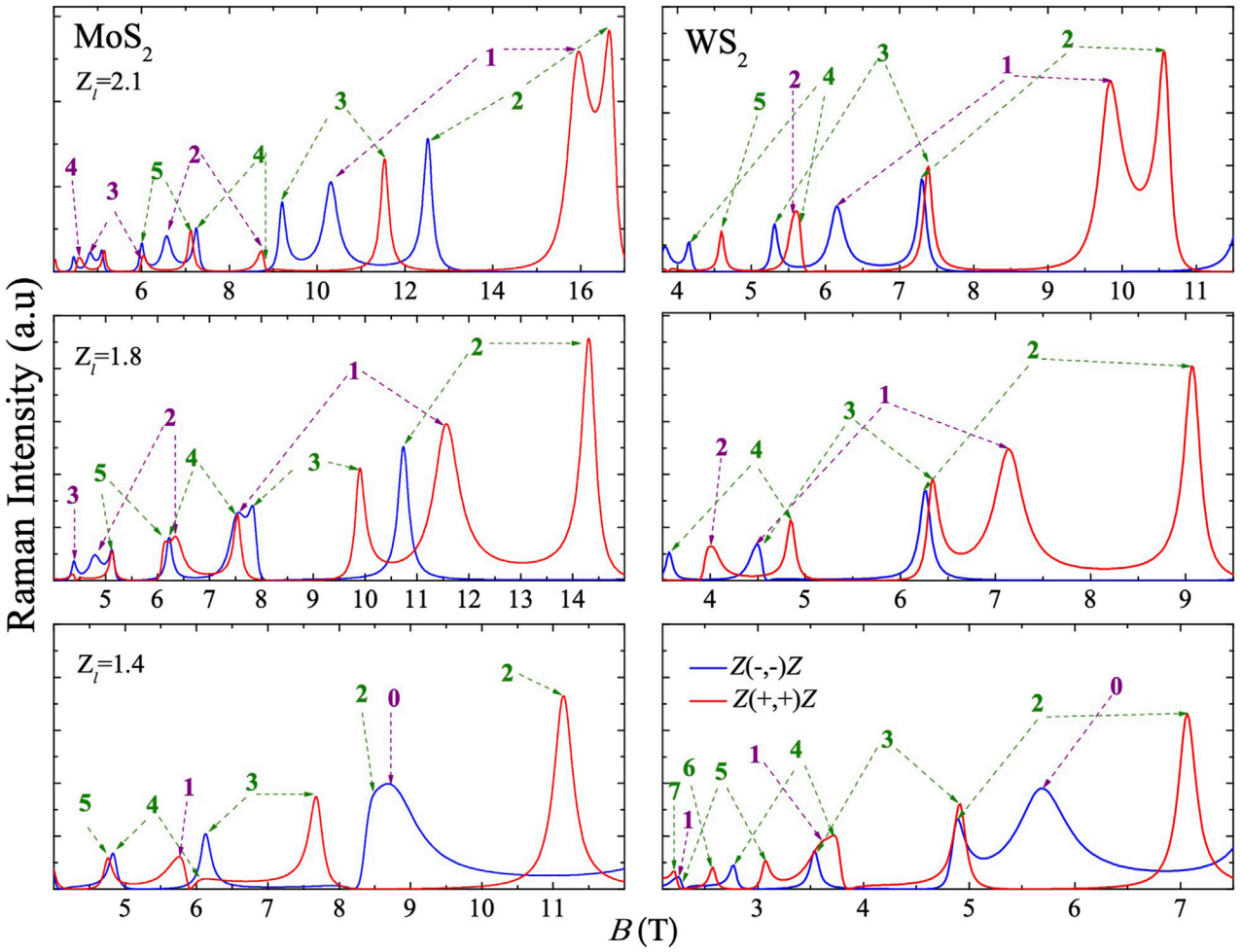

FIGURE 3
Raman intensity in two scattering configurations $\bar{Z}(\sigma^+,\sigma^+)Z$ (red lines) and $\bar{Z}(\sigma^-,\sigma^-)Z$ (blue lines) for ML MoS_2 and WS_2 as a function of B at three values of the parameter $Z_l = (\hbar\omega_l - E_g))/\hbar\omega_{A_1} = 2.1$, 1.8, and 1.4 (laser energy $\hbar\omega_l = 1.954$, 1.939, and 1.919 eV and 2.095, 2.08, and 2.005 eV for MoS_2 and WS_2, respectively). Dashed lines label the incoming (olive) and outgoing (purple) resonances for the EHP Landau level N.

$$W_{\rm FI}^{\rm DP} \propto \sum_{\mu_1,\mu_2} \delta_{N_{2e},N_{2h}}\delta_{s_{2e},s_{2h}}\left(\frac{\delta_{\mu_1,\mu_2}-\delta_{\mu_1,\mu_2}}{\left[\hbar\omega_s-\epsilon_{\mu_2}+i\delta\right]\left[\hbar\omega_l-\epsilon_{\mu_1}+i\delta\right]}\right)\delta_{N_{1e},N_{1h}}\delta_{s_{1e},s_{1h}}. \tag{5}$$

Consequently, for a ML TMD, it follows from Equation 5 that the contribution of the 2D long-range electric field (linked to the longitudinal optical phonon) to the Raman intensity, $dI^{\rm PF}/d\Omega$, vanishes. As discussed in Ref. [31], a backscattering geometry with oblique incidence is necessary for enhancing the in-plane phonon wave vector, where the 2D PF one-phonon mechanism is allowed.

2.3 Deformation potential

Using Eqs 3, 4 and Supplementary Equation S10, we get

$$W_{\rm FI}^{\rm DP} \propto l_c^{-2}\sum_N \frac{\delta_{q_x,0}\delta_{q_x,0}}{\left[\mathcal{E}_l-\hbar\omega_c\left(N+\frac{1}{2}\right)\right]\left[\mathcal{E}_s-\hbar\omega_c\left(N+\frac{1}{2}\right)\right]}, \tag{6}$$

where $\mathcal{E}_{l(s)} = \hbar\omega_{l(s)} - E_g - \mu_B B(g_e - g_h)m_s + i\delta$; $\omega_s = \omega_l - \omega_{A_1}$ and $m_s = \pm\frac{1}{2}$ for spin-up and spin-down; $g_e - g_h$ the EH g-factor; μ_B the Bohr magneton; and ω_c the EH–cyclotron frequency with the reduced mass given by $\mu_{\rm EH}^{-1} = m_e^{-1} + m_h^{-1}$. Upon inserting Eq. 6 into Eq. 2, the Raman scattering efficiency per unit solid angle $d\Omega$ takes the form

$$\frac{dI^{\rm DP}}{d\Omega} = I_0 l_c^{-4}\left|\sum_N \frac{1}{\left[\mathcal{E}_l-\hbar\omega_c\left(N+\frac{1}{2}\right)\right]\left[\mathcal{E}_s-\hbar\omega_c\left(N+\frac{1}{2}\right)\right]}\right|^2, \tag{7}$$

where

$$I_0 = \left(\frac{\omega_s}{\omega_l}\right)^2 \frac{\eta_s^2}{\pi^4 c^4}\frac{e^4a^4t^4}{\hbar^2}\frac{(D_c-D_v)^2}{2\rho_m\hbar\omega_{A_1}}. \tag{8}$$

2.3.1 Band parameters

Employing the $\bar{Z}(\sigma_s^{\pm}\sigma_l^{\pm})Z$, configurations, we select different spin orientations and interband optical transitions $V_i \leftrightarrow C_j$ (i, j =1,2). For a fixed laser energy $\hbar\omega_l > E_g$, the sets of the magnetic field values, for which the incoming, $\{B_N^{(in)}\}$, and outgoing, $\{B_N^{(out)}\}$, resonances occur, are given by

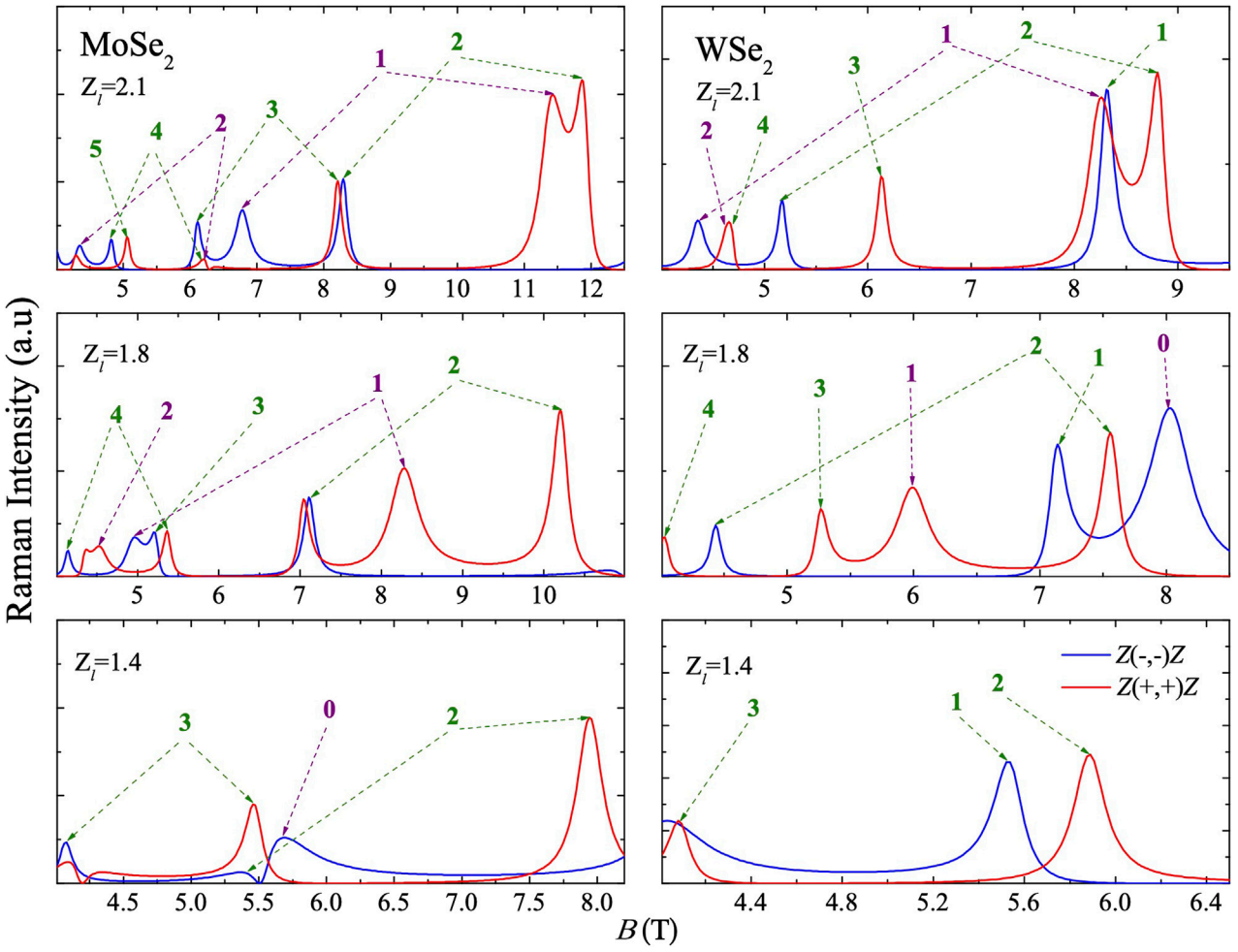

FIGURE 4
Same as Figure 3 for $MoSe_2$ ($\hbar\omega_l$ =1.652, 1.643, and 1.631 eV) and WSe_2 ($\hbar\omega_l$ = 1.823, 1.814, and 1.802a eV).

$$\hbar\omega_l - E_{gV_i\to C_j} = \mu_B g m_s B_N^{(in)} + \hbar\omega_c^{(V_i\to C_j)}\left(B_N^{(in)}\right)\left[N+\frac{1}{2}\right], \quad (9)$$

$$\hbar\omega_l - E_{gV_i\to C_j} - \hbar\omega_{A_1} = \mu_B g m_s B_N^{(out)} + \hbar\omega_c^{(V_i\to C_j)}\left(B_N^{(out)}\right)\left[N+\frac{1}{2}\right], \quad (10)$$

with the conditions $B_N^{(in)} \geq 0$ and $B_N^{(out)} \geq 0$. 9, 10, N = 0, 1, 2, ... $g = g_e - g_h$, $E_{gV_i\to C_j}$, and $\hbar\omega_c^{(V_i\to C_j)}$ are the gap energy and the cyclotron frequency for the transition between the valence band V_i and the conduction band C_j (i, j = 1,2). The above relations allow for a straightforward determination of the important band parameters of the TMD materials.

For ML MoX_2 materials in the $\bar{Z}(\boldsymbol{\sigma}_s^-, \boldsymbol{\sigma}_l^-)Z$ configuration, the main contribution corresponds to the transition between the V_1 and C_2 bands at the K-valley of the BZ. The input of the K'-valley for the $V_1 \leftrightarrow C_2$ transition is negligible for laser energies in the vicinity of the gap energy. Typical 2D TMD structures present a valence band spin-splitting $\Delta_{V_1-V_2}$ ranging between 150 and 480 meV. In the $\bar{Z}(\boldsymbol{\sigma}^+, \boldsymbol{\sigma}^+)Z$ configuration, the situation is reverse; the direct optical transition is between the $V_2 \leftrightarrow C_1$ bands (see Figure 2), and the contribution of the K-valley does not play a significant role. Employing the Faraday $\bar{Z}(\boldsymbol{\sigma}^\pm, \boldsymbol{\sigma}^\pm)Z$ configurations, we select different electron and hole effective masses, and spin orientation in the Raman spectra. The effective band parameters, phonon frequency, Landé g -factor, lattice constant, and EH-phonon DP coupling constant for MoX_2 and WX_2 families are summarized in Table 1. In the WX_2 compounds, the spin sub-bands of the conduction band shown in Figure 2 are reversed; hence, there are the $V_1 \leftrightarrow C_1$ and $V_2 \leftrightarrow C_2$ allowed optical transitions for $\bar{Z}(\boldsymbol{\sigma}^-, \boldsymbol{\sigma}^-)Z$ and $\bar{Z}(\boldsymbol{\sigma}^+, \boldsymbol{\sigma}^+)Z$, respectively. Figure 3 shows the resonant Raman profiles calculated according to Eq. 7 as a function of B in MoS_2 and WS_2. The blue (red) solid lines correspond to the backscattering configuration $\bar{Z}(\boldsymbol{\sigma}^-, \boldsymbol{\sigma}^-)Z$ ($\bar{Z}(\boldsymbol{\sigma}^+, \boldsymbol{\sigma}^+)Z$). Following Eqs 9, 10, the incoming and outgoing resonances due to the interband magneto-optical transitions for different Landau N are indicated by olive and purple dashed lines, respectively. In evaluation of the Raman intensities, we assume a constant broadening ($\delta/\hbar\omega_{A_1}$ = 2) independent of the magnetic field and the Landau quantum number. From Figure 3,

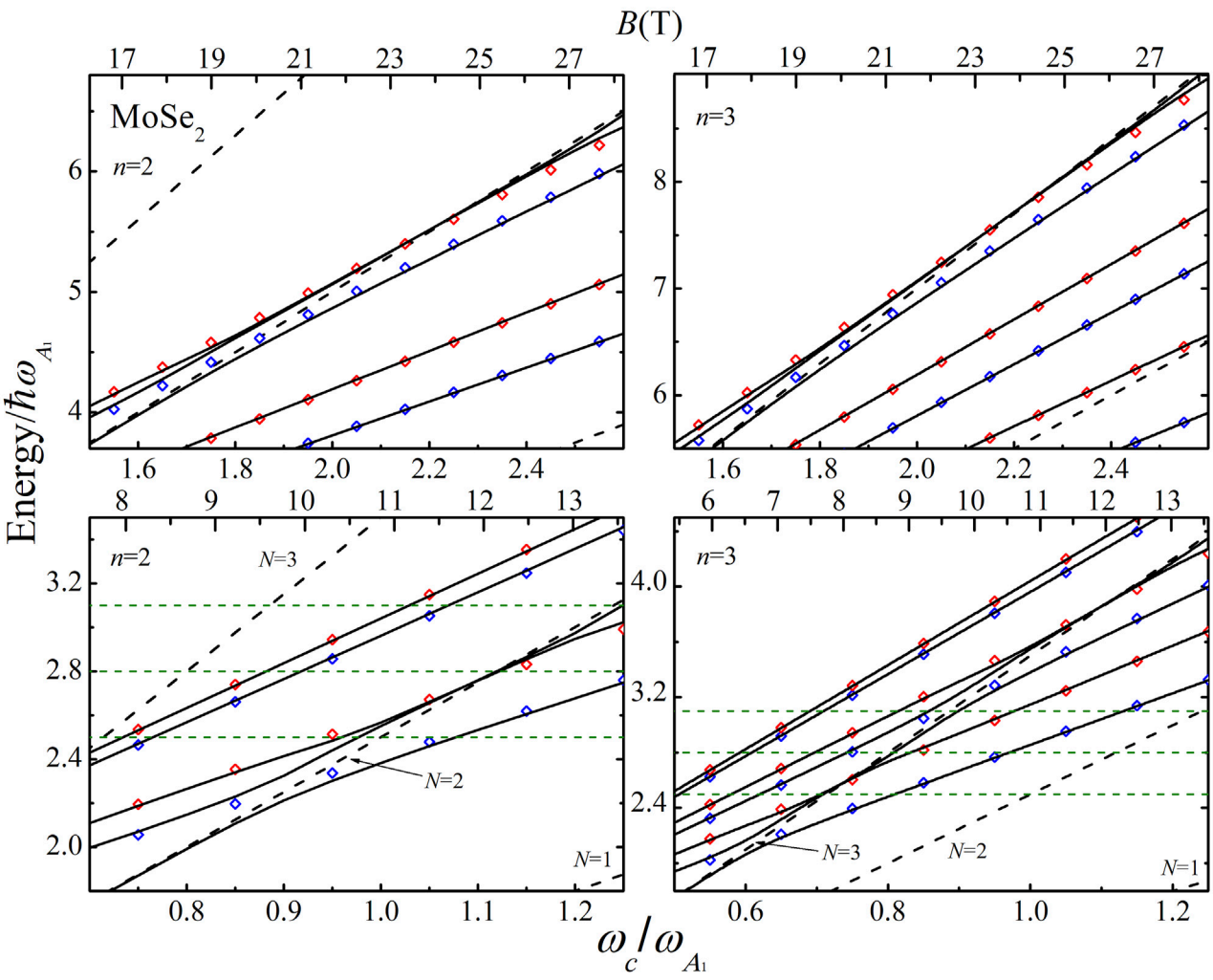

FIGURE 5
MP energy (solid lines) as a function of the relative cyclotron frequency ω_c/ω_{A_1} in a ML $MoSe_2$ for the states $n = 2$ and 3. The $V_1 \leftrightarrow C_2$ optical transition is considered.

it is seen that the resonance profile increases as $l_c^{-4} \sim B^2$ and the characteristic oscillatory behavior occurs due to a sequence of incoming and outgoing resonances as a function of the magnetic field. The resonance conditions are obtained for the magnetic fields satisfying Eqs 9, 10. For MoS_2, the peaks of the magneto-Raman spectra for a given quantum number N are located at lower magnetic fields in the configuration $\bar{Z}(\boldsymbol{\sigma}^-, \boldsymbol{\sigma}^-)Z$ than in the configuration $\bar{Z}(\boldsymbol{\sigma}^+, \boldsymbol{\sigma}^+)Z$. This fact reveals the dependence of the effective masses on the optical selection rules in MoX_2 versus WX_2 families, and the value of the reduced effective mass for the $\boldsymbol{\sigma}^-$ polarization is larger than that in the $\boldsymbol{\sigma}^+$ case (see Table 1). Therefore, ω_c for the (-,-) configuration is larger than that for the (+,+) configuration, and the resonances appear at lower B values as follows from Eqs 9, 10. The same calculations were performed for $MoSe_2$ and WSe_2 (see Figure 4). When comparing the Raman spectra of the MoX_2 versus WX_2 families, it is clear that the peak positions for a given N are shifted in the molybdenum-based materials to a higher energy in comparison to the tungsten-based ones, reflecting the band structure and the inherent symmetry of each family.

2.3.1.1 Electron–hole g-factor

In the $(\pm, \pm)$ configurations, the electron–hole g-factor can be written as

$$g_e - g_h = \frac{4(N + 1/2)}{B_2 + B_1}\left[B_2\frac{m_0}{\mu_{(V_1 \to C_2)}} - B_1\frac{m_0}{\mu_{(V_2 \to C_1)}}\right], \qquad (11)$$

with B_1 and B_2 being the field values, where the resonances occur (see Eqs 9, 10). From Eq. 11, it follows that the value of the $g_e - g_h$ factor depends on the effective masses of the K- and K'-valleys. Thus, observations of the incoming and outgoing resonances in the magneto-Raman spectrum can provide information on the band parameters of the ML TMDs as a function of the applied field B.

2.4 Polaron effects

MP effects on Raman scattering were investigated for a long time in nanostructures [32, 33]. The discrete nature of the Landau level transitions and their MP resonances in graphene were clearly

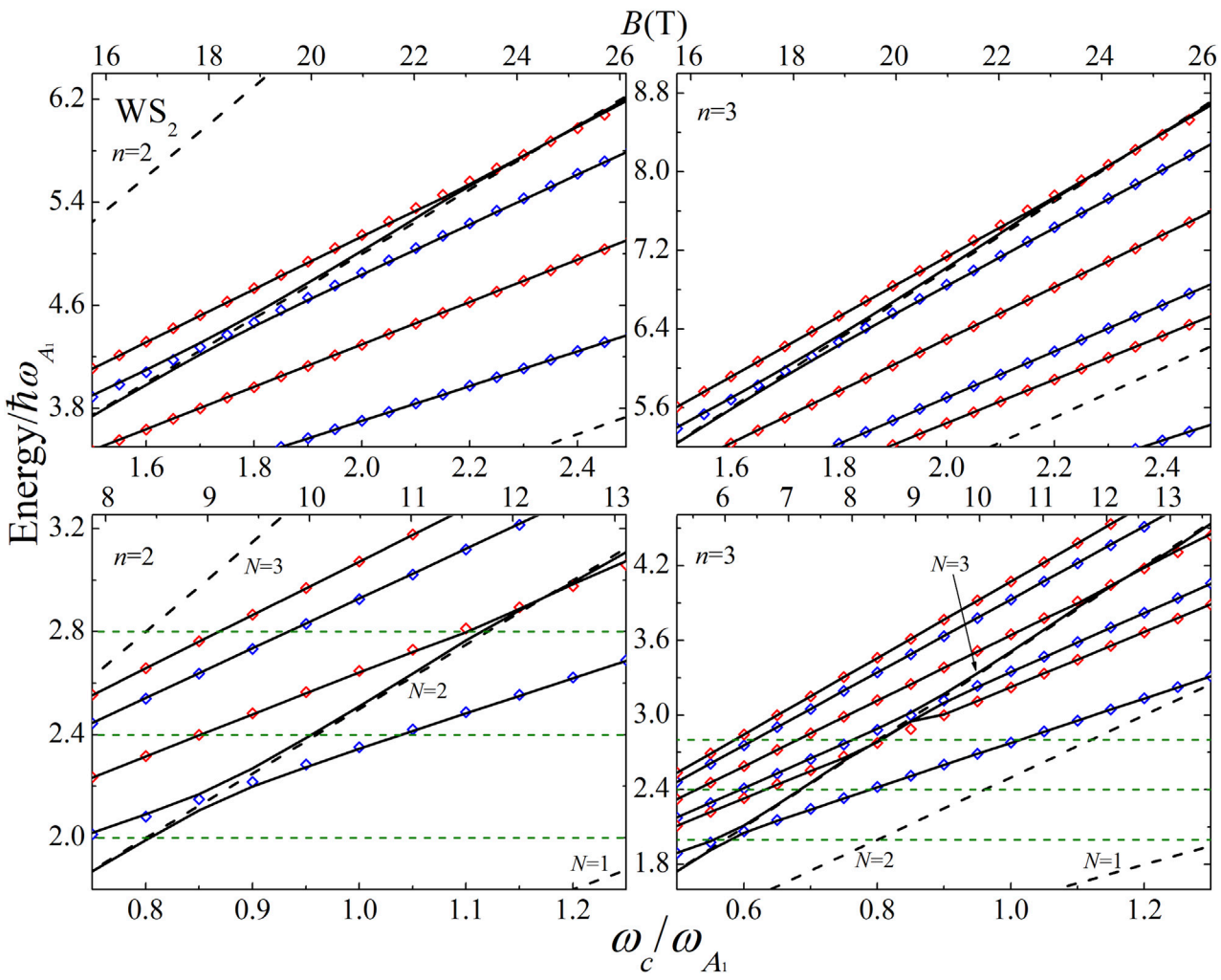

FIGURE 6
Same as Figure 5 for WS_2. The $V_1 \leftrightarrow C_1$ optical transition is considered.

identified by Raman spectroscopy. In a simple picture of two Landau levels, separated by the optical phonon energy, the MP resonance is split into two branches. This fact is not true in materials, where the magneto-optical transitions occur between the valence and conduction bands with similar effective masses. Generally, no part of the MP self-energy can be decoupled into two independent contributions originating from the conduction and valence bands: the overlap of the electron and hole Landau states must be taken into account. The self-energy, as displayed in Supplementary Equation S14, implies a summation over all Landau levels in the conduction and valences bands.

In the evaluation of the scattering efficiency shown in Figures 3, 4, the MP effects are not taken into account. In the first-order resonant Raman scattering, the impinging light and the scattered light lead to the creation and annihilation of electrons and holes simultaneously in the same quantum Landau state; therefore, at a certain laser energy and B, the MP resonances should be involved in the light scattering process. Hence, the free EHP states in a magnetic field embedded in the Green's function $G^{(0)}$ are no longer a correct set of states valid for the description of resonant magneto-Raman scattering. In Eq. 3, the bare Green's function $G_{\mu}^{(0)}(E)$, that appears in Figure 1B, must be replaced by summing the subset of Feynman diagrams considering the interaction of the EHP Landau states with the optical phonons. The procedure leads to the renormalized Green's function, $G_{\{\mu\}}(E) = G_{n(N)}(E)$ [19, 20], where $n(N)$ labels the MP states. The complex-valued function $E(B)$, present in Supplementary Equation S21, provides the MP energy $\Re\{E\} = \hat{\epsilon}_{n(N)}$ (see Section 3 in Supplementary Material). For a fixed N value, the quantum number n labels the EHP quasi-particle states, i.e., the renormalized Landau state and the corresponding excited states as a function of B. The EHP MP spectra for the n =2 and 3 states of a ML $MoSe_2$ and a ML WS_2 are displayed in Figures 5, 6. For the calculation, we employed the materials and parameters listed in Table 1. In the figures, the bare excited states for electrons, $\hbar\omega_e^{(exc)} = \hbar\omega_{A_1} + \hbar\omega_{c_e}(p_e + 1/2) + \hbar\omega_{c_h}(N + 1/2)$, and for holes, $\hbar\omega_h^{(exc)} = \hbar\omega_{A_1} + \hbar\omega_{c_e}(N + 1/2) + \hbar\omega_{c_h}(p_h + 1/2)$, ($p_e$, p_h = 0,1,2,. . .,N-1), are symbolized by blue and red empty diamonds, respectively, while the uncoupled Landau levels N are symbolized by dashed lines. From the figures, the MP resonances due to the electron–phonon and hole–phonon interaction are clearly seen. For each EPH Landau level N, there are three branches. The anti-crossing points are sited at the cyclotron resonance

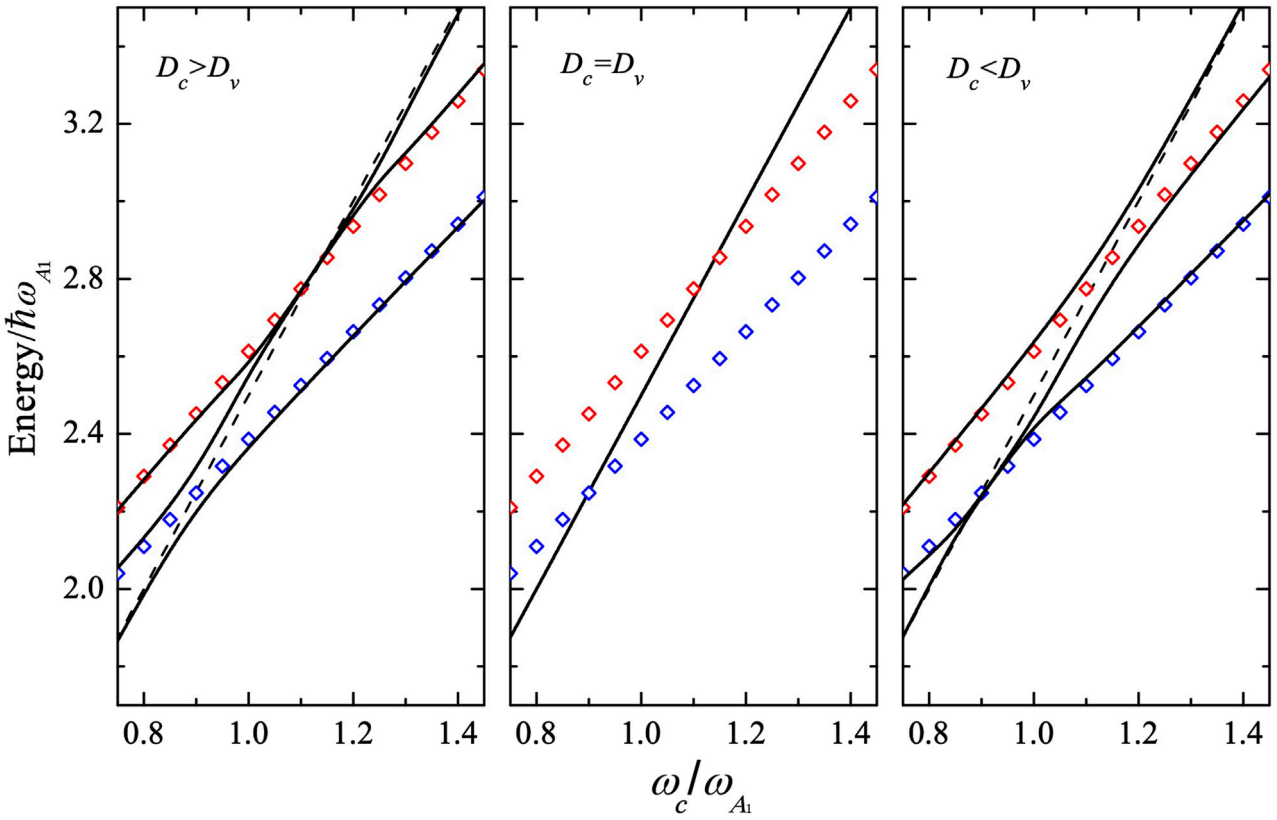

FIGURE 7
MP energy $\hat{\epsilon}_2$ as a function of B for $MoSe_2$ at three values of D_c/D_v.

transition energies $\omega_{c_i}/\omega_{A_1} = 1/3, 1/2$ and 1 for the conduction $(i = e)$ and valence $(i = h)$ bands, respectively. In particular, for $n = 2$, there are four avoided-crossing levels, and for $n = 3$, there exist six such levels. In $MoSe_2$ (WS_2), the crossing points are at $\omega_c/\omega_{A_1} = 0.61, 0.91, 1.81$ (0.58, 0.87, 1.74) and 0.7, 1.1, 2.2 (0.78, 1.17, 2.34) for the electron and hole, respectively. Comparing spectra of Figures 5, 6, we find that the magnetic fields, where anti-crossings occur, are higher in $MoSe_2$ than those in WS_2, while the gap is also greater, reflecting the fact that the electron-deformation potential is smaller in the WX_2 family than in the MoX_2 one. For the hole at each anti-crossing point, there exists a superposition between the renormalized electron and hole excited states. This effect is due to the values of the deformation potential D_c and D_v (see Table 1; Supplementary Equation S22). The ratio $D_v/D_c < 1$ provokes a superposition of the electron and hole excited states at higher values of ω_c/ω_{A_1} (0.7, 1.1, 2.2 and 0.78, 1.17, 2.34 for $MoSe_2$ and WS_2, respectively). To visualize this effect, Figure 7 highlights the MP for n =2 as a function of the ratio $R = D_c/D_v$. If $R > 1$, the anti-crossing takes place at the electron cyclotron frequency $\omega_{c_e}/\omega_{A_1} = 1/2$ $(\omega_c/\omega_{A_1} = 0.91)$, while for the hole cyclotron frequency $\omega_{c_h}/\omega_{A_1} = 1/2$ $(\omega_c/\omega_{A_1} = 1.1)$, a crossover occurs between the renormalized excited states of the electron and hole. For $R < 1$, the situation is reversed, the gap opens at the hole cyclotron frequency, $\omega_{c_h}/\omega_{A_1} = 1/2$, and the electron–hole superposition occurs at $\omega_{c_e}/\omega_{A_1} = 1/2$. In the specific case of $D_c = D_v$, the MP quasi-particle is absent, and the undressed Landau level $N = 2$ is recovered.

2.5 RMPRS efficiency

All of the previously discussed effects of the MP spectrum are reflected in the Raman intensity. Replacing the Green's function $G_\mu^{(0)}$ by the "dressed" Green's function $G_{n(N)}$ in Eq. 3, we derive the resonant MP Raman efficiency

$$\frac{dI^{\rm DP}}{d\Omega} \propto B^2 \left| \sum_{n(N)} \frac{1}{\left[\hbar\omega_l - E_g - E_{n(N)}(B) - i\delta\right]\left[\hbar\omega_l - E_g - \hbar\omega_{A_1} - E_{n(N)}(B) - i\delta\right]} \right|^2, \tag{12}$$

where $E_{n(N)} = \hat{\epsilon}_{n(N)} + i\Gamma_{n(N)}$ is the solution of the coupled Supplementary Equations S22, S23, and the sum for each n is over all MP states, i.e., the renormalized Landau level N and excited states with $p_e = 0, 1, N-1$ and $p_h = 1, \ldots, N-1$. Eq. 12 is isomorphic to Eq. 7, with MP effects included. The main difference lies in the replacement of the bare Landau levels $\hbar\omega_c(N + 1/2)$ by the new set of the quasi-particle excitation energies $E_{n(N)}$. As stated previously, the MP energies are the fundamental conceptual ingredient of the Raman scattering efficiency. By scanning the Raman intensity with the field B and different incident laser energies, we are able to study the EHP spectrum and the properties of the MP. Figures 8, 9 represent the resonant MP Raman efficiency profiles for a ML $MoSe_2$ and a ML WS_2. For the numerical evaluations, we employ the data in Table 1 for the scattering configuration $\bar{Z}(\boldsymbol{\sigma}^-, \boldsymbol{\sigma}^-)Z$, assuming δ = 1 meV and disregarding the Zeeman splitting. The resonant profiles

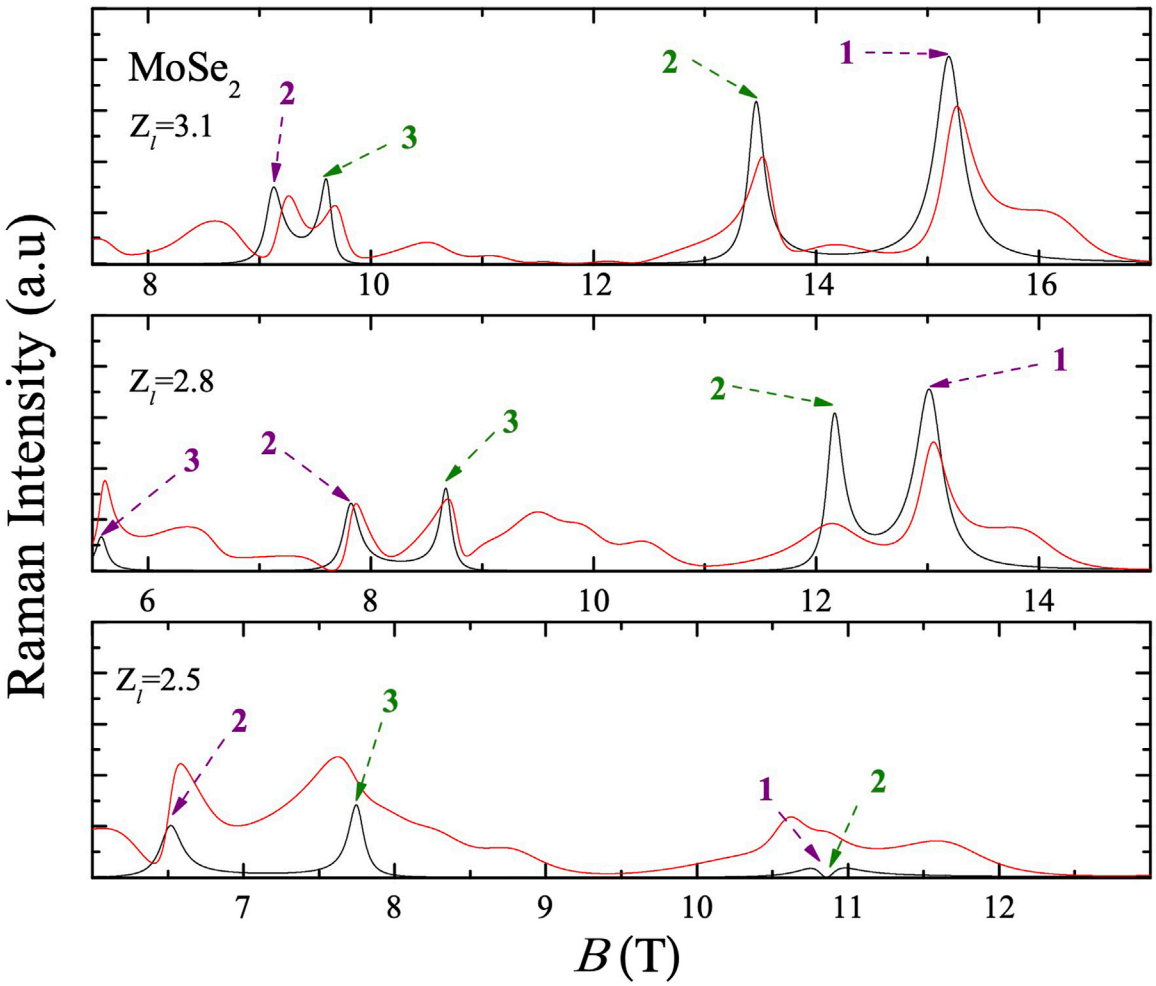

FIGURE 8
MP Raman scattering efficiency (red solid line) as given by Eq. 12 for a ML $MoSe_2$ in $\bar{Z}(\boldsymbol{\sigma}^-,\boldsymbol{\sigma}^-)Z$ backscattering configuration as a function of B at Z_l = 2.5, 2.8, and 3.1 ($\hbar\omega_l$ = 1.6635, 1.6723, and 1.6811 eV). Black solid lines show the Raman intensity without the MP effect. The incoming and outgoing resonances for the Landau level N are indicated by the green and violet arrows, respectively. In the calculation, the values of D_c = 5.2 eV [42] and D_v = 4.9 eV [43] are used.

are evaluated for the relative laser energies Z_l = 2.5, 2.8, 3.1 and 2.0, 2.4, 2.8 in $MoSe_2$ and WS_2, respectively. The positions of the resonance peaks occur at different values of the magnetic field values due to the A_1-phonon energies, 29.4 meV versus 51 meV in $MoSe_2$ and WS_2, respectively. For a fixed value of the relative laser frequency, the resonances may or may not be close to the avoided-crossing point of certain excitation branches. In the range of the magnetic field values near anti-crossings, the Landau levels are strongly renormalized by the A_1'-EPI. For a better analysis of the results shown in Figures 8, 9, the values of Z_l employed for the evaluation of the RMPRS intensity are indicated by green dotted lines in the MP spectra of $MoSe_2$ and WS_2 (Figures 5, 6). For example, the structure manifested in Figure 8 at Z_l = 2.5 in the range 10 T < B < 12 T represents the incoming resonances for three excitation branches of the MP energy spectrum. From Figure 5, it follows that these branches are near the avoided-crossing point $\hbar\omega_{c_e}/\hbar\omega_{A_1}$ = 1/2. The resonances correspond to the renormalized hole (B = 10.4 T) and electron (B = 10.6 T) excited states with p_h, p_e = 0, next to the renormalized Landau level N = 2 (B = 11.7 T). As seen in the spectrum of Figure 5, there are no other contributions to the Raman profile, while for B < 9 T, the main contribution to $dI^{\rm DP}/d\Omega$ is provided by the n = 3 MP states. Namely, there exists a set of incoming resonances in the Raman profile for the N = 3 Landau level at B = 7.69 T as well as the electron and hole renormalized excited states with p_e = 0, 1, 2 (B = 8.79, 6.73, 5.5 T) and p_h = 0, 1, 2 (B = 7.66, 6.29, 5.35 T). The maximum in Figure 8 corresponds to the contribution of the renormalized Landau energy N = 3 at B = 7.69 T and the hole excited state p_h = 0 at B = 7.66 T (see the MP spectrum in Figure 5). Interestingly, there are more contributions to the Raman intensity due to the states with n = 2 and p_e = p_h = 1 (B = 7.97, 8.3 T). The same analysis is performed for other materials and laser energies. Thus, for WS_2 at Z_l = 2.8, the maximum in the Raman profile corresponds to the renormalized Landau level N =2 (B = 11.68 T) and the excited states of the polaron quasi-particle p_h = 0 (B = 11.55 T) (see the MP spectrum in Figure 6). Importantly, in the RMPRS, given by Eq. 12, there are also manifestations of the outgoing resonances. Therefore, there is the same set of MP states contributing to the Raman profile, but now

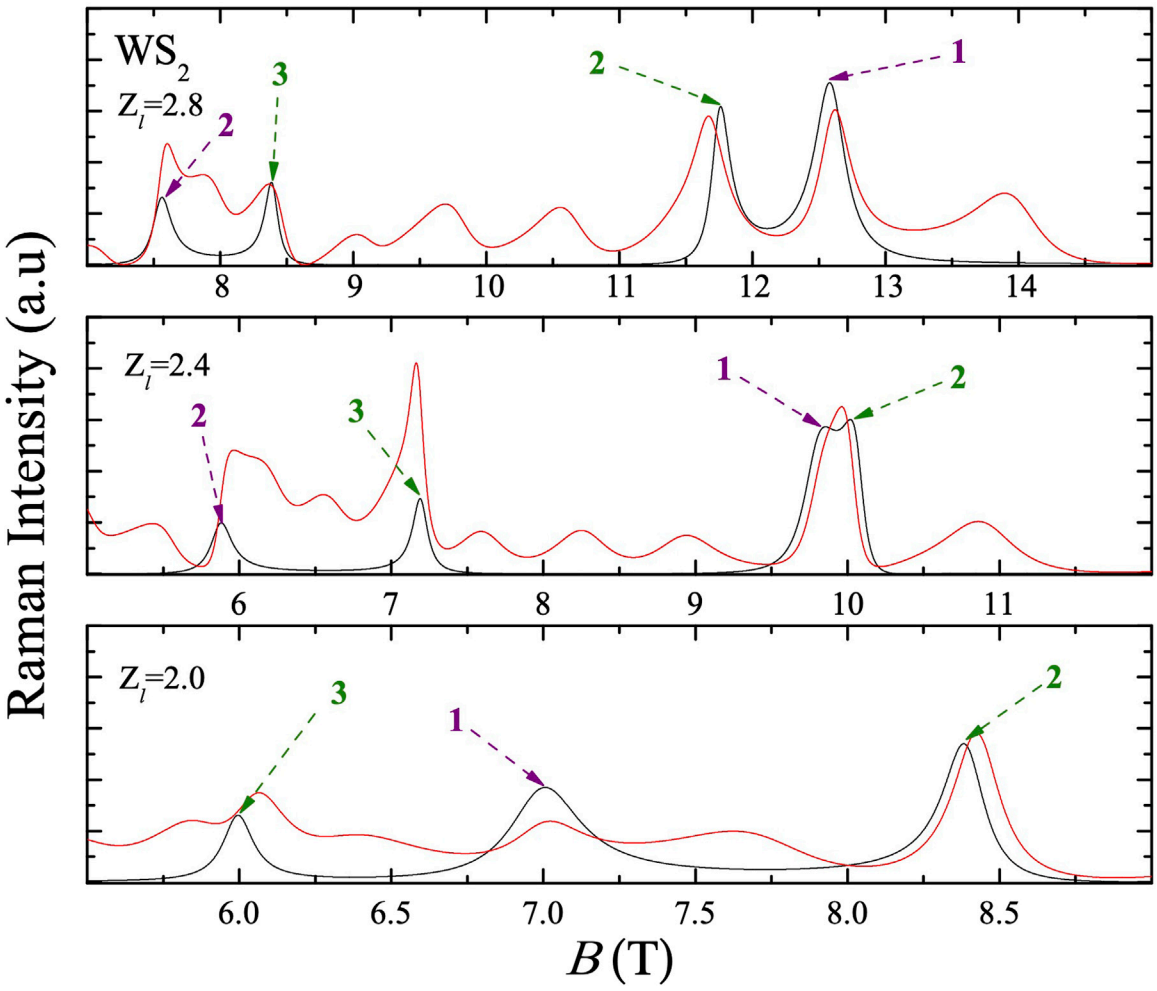

FIGURE 9
Same as Figure 8 for WS_2 at Z_l = 2.0, 2.4, and 2.8 ($\hbar\omega_l$ = 2.092, 2.1124, and 2.1328 eV). The values of D_c = 3.1 eV [42] and D_v = 2.3 eV [43] are employed.

shifted by the energy of an optical phonon. This is the case for the line shown in Figure 9 for Z_l = 2.0 at B= 7.1 T, which is associated with the outgoing resonance of the N = 1 Landau dressed state.

3 Conclusion and outlook

We have calculated the one-phonon magneto-resonant light scattering due to the out-of-plane A_1-phonon in ML TMD materials. The Raman efficiency in the backscattering configurations, $\bar{Z}(\boldsymbol{\sigma}^{\pm}, \boldsymbol{\sigma}^{\pm})Z$, represented by Eq. 7, provides a direct experimentally accessible information on the band structure. Processing the set of incoming and outgoing resonances that correspond to different interband magneto-optical transitions, as given by Eqs 9, 10 together with Eq. 11 for the EH g-factor, provides a powerful tool to extract the information of the principal band parameters at the K- and K'-valleys as a function of B. It is shown that the Raman intensity increases as B^2, exhibiting oscillations following the Landau transitions of the EHP. The theoretical model is extended onto the B range, where the MP effects play the main role in the formation of the Raman profile. The renormalized Landau levels are obtained by solving the equation for the self-energy operator due to the A_1'—DP interaction. A compact mathematical expression for the MP quasi-particle energy (Supplementary Equation S22) and its lifetime broadening (Supplementary Equation S23), which are essential for the Raman intensity, is provided. We have further presented a theoretical analysis of the MP resonances in a ML $MoSe_2$ and a ML WS_2. The unique characteristics of the conduction and valence bands and their contributions in the formation of the MP quasi-particle are revealed (see Figures 5, 6). The relative contributions of the electron and hole to the MP formation depend on the optical DP values. An analytical equation for RMPRS intensity as a function of the magnetic field (Eq. 12) is provided, allowing for the analysis of the MP formation in different ranges of the field B and the incoming laser energy. A central result of the present paper is the proof that the magneto-Raman efficiency is a fingerprint of the 2D MP excitation branches (see Figures 8, 9). The fundamental findings of this paper are of key importance for emerging novel electronic, optoelectronic [34, 35] and photonic devices [36], gas sensors [37], quantum-mechanical tunneling devices [38], tuning photodetectors by the magnetic field [39, 40], and controlling radiative lifetimes in TMD materials by an applied magnetic field [41], among numerous potential applications. The observation of the

RMPRS is a heuristically important starting point for further basic research on a wide range of the magneto-optical properties of TMDs. As desirable developments, there are extensions of the present formalism to bilayer and Moiré structures, MP effects in multi-phonon resonant Raman scattering, and magneto-hot-luminescence.

Data availability statement

The original contributions presented in the study are included in the article/Supplementary Material; further inquiries can be directed to the corresponding author.

Author contributions

CT-G: Conceptualization, Formal analysis, Investigation, Funding acquisition, Writing–original draft. DGS-P: Data curation, Formal analysis, Investigation, Writing–review and editing. DVT: Data curation, Formal analysis, Investigation, Writing–review and editing. GEM: Investigation, Writing–review and editing. VMF: Formal analysis, Investigation, Writing–review and editing.

Funding

The author(s) declare that financial support was received for the research, authorship, and/or publication of this article. GEM and CT-G declare partial financial support from Brazilian agencies, Fundação de Amparo a Pesquisa do Estado de São Paulo (FAPESP, Proc. 304404/2023-3, 2022/08825-8, and 2020/07255-8) and Conselho Nacional de Desenvolvimento Científico e Tecnológico (CNPq, Proc. 302007/2019-9).

Acknowledgments

CT-G acknowledges the Alexander von Humboldt Foundation for providing research fellowship and to the Leibniz Institute for Solid State and Materials Research Dresden for hospitality.

Conflict of interest

The authors declare that the research was conducted in the absence of any commercial or financial relationships that could be construed as a potential conflict of interest.

The author(s) declared that they were an editorial board member of Frontiers, at the time of submission. This had no impact on the peer review process and the final decision.

Publisher's note

Supplementary material

The Supplementary Material for this article can be found online at: https://www.frontiersin.org/articles/10.3389/fphy.2024.1440069/full#supplementary-material

References

1. Ruf T, Phillips RT, Trallero-Giner C, Cardona M. Resonant magneto-Raman scattering in GaAs. *Phys Rev B* (1990) 41:3039–3047. doi:10.1103/PhysRevB.41.3039

2. Ruf T, Phillips RT, Cantarero A, Ambrazeviius G, Cardona M, Schmitz J, et al. Resonant Raman scattering and piezomodulated reflectivity of InP in high magnetic fields. *Phys Rev B* (1989) 39:13378–13388. doi:10.1103/PhysRevB.39.13378

3. McDonnell LP, Viner JJS, Ruiz-Tijerina DA, Rivera P, Xu X, Fal'ko VI, et al. Superposition of intra- and inter-layer excitons in twistronic $MoSe_2/WSe_2$ bilayers probed by resonant Raman scattering. *2D Mater* (2021) 8:035009. doi:10.1088/2053-1583/abe778

4. Ji J, Zhang A, Fan J, Li Y, Wang X, Zhang J, et al. Giant magneto-optical Raman effect in a layered transition metal compound. *Proc Natl Acad Sci U S A* (2016) 113:2349–2353. doi:10.1073/pnas.1601010113

5. Scheuschner N, Gillen R, Staiger M, Maultzsch J. Interlayer resonant Raman modes in few-layer MoS_2. *Phys Rev B* (2015) 91:235409. doi:10.1103/PhysRevB.91.235409

6. Trallero-Giner C, Menéndez-Proupin E, Morell ES, Pérez-Álvarez R, Santiago-Pérez DG. Phenomenological model for long-wavelength optical modes in transition metal dichalcogenide monolayer. *Phys Rev B* (2021) 103:235424. doi:10.1103/PhysRevB.103.235424

7. Zhang X, Qiao X-F, Shi W, Wu J-B, Jiang D-S, Tan P-H. Phonon and Raman scattering of two-dimensional transition metal dichalcogenides from monolayer, multilayer to bulk material. *Chem Soc Rev* (2015) 44:2757–2785. doi:10.1039/C4CS00282B

8. Gurevich VL, Firsov YA. On the theory of the electrical conductivity of semiconductors in a magnetic field. i. *Sov Phys JETP* (1961) 13:137.

9. Parfen'ev R, Shalyt S, Muzhdaba V. An experimental confirmation of magnetophonon resonance in n-type InSb. *Soviet Phys JETP* (1965) 20:294.

10. Puri S, Geballe T. Thermomagnetic effects in the quantum region. *Semiconductors and Semimetals* (1966) 1:203–64. Elsevier.

11. Eaves L, Guimaraes P, Portal J. Hot-electron magnetophonon spectroscopy on micron- and sub-micron-size n^+nn^+GaAs structures. *J Phys C: Solid State Phys* (1984) 17:6177–6190. doi:10.1088/0022-3719/17/34/018

12. Dresselhaus G, Kip AF, Kittel C. Cyclotron resonance of electrons and holes in silicon and germanium crystals. *Phys Rev* (1955) 98:368–384. doi:10.1103/PhysRev.98.368

13. Bass FG, Levinson IB. Cyclotron-phonon resonance in semiconductors. *Sov Phys JETP* (1965) 49:914–924.

14. López V, Comas F, Trallero-Giner C, Ruf T, Cardona M. Resonant electron-phonon coupling: magnetopolarons in inp. *Phys Rev B* (1996) 54:10502. doi:10.1103/PhysRevB.54.10502

15. Portal JC, Perrier P, Houlbert C, Askenazy S, Nicholas RJ, Stradling RA. Impurity-associated magnetophonon resonance in n-type silicon. *J Phys C: Solid State Phys* (1979) 12:5121–5143. doi:10.1088/0022-3719/12/23/02023/020

16. Wysmołek A, Plantier D, Potemski M, Słupiński T, Żytkiewicz ZR. Coupled plasmon–LO-phonon modes at high-magnetic fields. *Phys Rev B* (2006) 74:165206. doi:10.1103/PhysRevB.74.165206

17. Faugeras C, Amado M, Kossacki P, Orlita M, Kühne M, Nicolet AAL, et al. Magneto-Raman scattering of graphene on graphite: electronic and phonon excitations. *Phys Rev Lett* (2011) 107:036807. doi:10.1103/PhysRevLett.107.036807

18. Goler S, Yan J, Pellegrini V, Pinczuk A. Raman spectroscopy of magneto-phonon resonances in graphene and graphite. *Solid State Commun* (2012) 152:1289–1293. Exploring Graphene, Recent Research Advances. doi:10.1016/j.ssc.2012.04.020

19. Belitsky VI, Trallero-Giner C, Cardona M. Magnetopolaron effect in one-phonon resonant Raman scattering from bulk semiconductors: deformation potential. *Phys Rev B* (1993) 48:17861. doi:10.1103/PhysRevB.48.17861

20. Belitsky VI, Trallero-Giner C, Cardona M. Magnetopolaron effect in one-phonon resonant Raman scattering from bulk semiconductors: fröhlich interaction. *Phys Rev B* (1994) 49:11016–11020. doi:10.1103/PhysRevB.49.11016

21. Faugeras C, Amado M, Kossacki P, Orlita M, Sprinkle M, Berger C, et al. Tuning the electron-phonon coupling in multilayer graphene with magnetic fields. *Phys Rev Lett* (2009) 103:186803. doi:10.1103/PhysRevLett.103.186803

22. Jia C, Jia D, Zhang H, Jiang D, Meng Y. Temperature dependence on energy-levels of surface-optical magnetopolaron in monolayer graphene on polar substrate under an external filed. *Phys Lett A* (2024) 509:129514. doi:10.1016/j.physleta.2024.129514

23. Stier AV, McCreary KM, Jonker BT, Kono J, Crooker SA. Exciton diamagnetic shifts and valley Zeeman effects in monolayer WS_2 and MoS_2 to 65 Tesla. *Nat Commun* (2016) 7:10643. doi:10.1038/ncomms10643

24. Yan J, Henriksen EA, Kim P, Pinczuk A. Observation of anomalous phonon softening in bilayer graphene. *Phys Rev Lett* (2008) 101:136804. doi:10.1103/PhysRevLett.101.136804

25. Zhao L, He R, Rim KT, Schiros T, Kim KS, Zhou H, et al. Visualizing individual nitrogen dopants in monolayer graphene. *Science* (2011) 333:999–1003. doi:10.1126/science.1208759

26. Loudon R. The Raman effect in crystals. *Adv Phys* (1964) 13:423–482. doi:10.1080/00018736400101051

27. Chamberlain MP, Trallero-Giner C, Cardona M. Theory of one-phonon Raman scattering in semiconductor microcrystallites. *Phys Rev B* (1995) 51:1680–1693. doi:10.1103/PhysRevB.51.1680

28. Kormányos A, Burkard G, Gmitra M, Fabian J, Zólyomi V, Drummond ND, et al. k p theory for two-dimensional transition metal dichalcogenide semiconductors. *2D Mater* (2015) 2:022001. doi:10.1088/2053-1583/2/2/0220012/2/022001

29. Glazov MM, Ivchenko EL. Valley orientation of electrons and excitons in atomically thin transition metal dichalcogenide monolayers (brief review). *JETP Lett* (2021) 113:7–17. doi:10.1134/S0021364021010033

30. Tarucha S, Okamoto H, Iwasa Y, Miura N. Exciton binding energy in gaas quantum wells deduced from magneto-optical absorption measurement. *Solid State Commun* (1984) 52:815. doi:10.1016/0038-1098(84)90012-70038-1098(84)90012-7

31. Trallero-Giner C, Santiago-Pérez DG, Vasilevskiy MI, Marques GE. Rydberg excitons and doubly resonant Raman scattering in transition-metal dichalcogenides. *The J Phys Chem C* (2024) 128:210. doi:10.1021/acs.jpcc.3c06303

32. Wang YJ, Nickel HA, McCombe BD, Peeters FM, Shi JM, Hai GQ, et al. Resonant magnetopolaron effects due to interface phonons in GaAs/AlGaAS multiple quantum well structures. *Phys Rev Lett* (1997) 79:3226. doi:10.1103/PhysRevLett.79.3226

33. Hameau S, Guldner Y, Verzelen O, Ferreira R, Bastard G, Zeman J, et al. Strong electron-phonon coupling regime in quantum dots: evidence for everlasting resonant polarons. *Phys Rev Lett* (1999) 83:4152. doi:10.1103/physrevlett.83.4152PhysRevLett.83.4152

34. Wang QH, Kalantar-Zadeh K, Kis A, Coleman JN, Strano MS. Electronics and optoelectronics of two-dimensional transition metal dichalcogenides. *Nat Nanotechnology* (2012) 7:699–712. doi:10.1038/nnano.2012.193

35. Tian H, Chin ML, Najmaei S, Guo Q, Xia F, Wang H, et al. Optoelectronic devices based on two-dimensional transition metal dichalcogenides. *Nano Res* (2016) 9:1543–1560. doi:10.1007/s12274-016-1034-9

36. McDonnell SJ, Wallace RM. Atomically-thin layered films for device applications based upon 2D TMDC materials. *Thin Solid Films* (2016) 616:482–501. doi:10.1016/j.tsf.2016.08.068

37. Huo N, Yang S, Wei Z, Li S-S, Xia J-B, Li J. Photoresponsive and gas sensing field-effect transistors based on multilayer WS_2 nanoflakes. *Scientific Rep* (2014) 4:5209. doi:10.1038/srep05209

38. Lu H, Seabaugh A. Tunnel field-effect transistors: state-of-the-art. *IEEE J Electron Devices Soc* (2014) 2:44. doi:10.1109/JEDS.2014.2326622

39. Chang Y-H, Zhang W, Zhu Y, Han Y, Pu J, Chang J-K, et al. Monolayer $MoSe_2$ grown by chemical vapor deposition for fast photodetection. *ACS Nano* (2014) 8:8582–8590. doi:10.1021/nn503287m

40. Lopez-Sanchez O, Lembke D, Kayci M, Radenovic A, Kis A. Ultrasensitive photodetectors based on monolayer MoS_2. *Nat Nanotechnology* (2013) 8:497–501. doi:10.1038/nnano.2013.100

41. Mak KF, Shan J. Photonics and optoelectronics of 2d semiconductor transition metal dichalcogenides. *Nat Photon* (2016) 10:216–26. doi:10.1038/nphoton.2015.282

42. Kaasbjerg K, Thygesen KS, Jacobsen KW. Phonon-limited mobility in n-type single-layer MoS_2 from first principles. *Phys Rev B* (2012) 85:115317. doi:10.1103/PhysRevB.85.115317

43. Jin Z, Li X, Mullen JT, Kim KW. Intrinsic transport properties of electrons and holes in monolayer transition-metal dichalcogenides. *Phys Rev B* (2014) 90:045422. doi:10.1103/PhysRevB.90.045422

44. Koperski M, Molas MR, Arora A, Nogajewski K, Bartos M, Wyzula J, et al. Orbital, spin and valley contributions to Zeeman splitting of excitonic resonances in $MoSe_2$, WSe_2 and WS_2 Monolayers. *2D Mater* (2018) 6:015001. doi:10.1088/2053-1583/aae14b

45. Deilmann T, Krüger P, Rohlfing M. *Ab initio* studies of exciton g factors: monolayer transition metal dichalcogenides in magnetic fields. *Phys Rev Lett* (2020) 124:226402. doi:10.1103/PhysRevLett.124.226402

46. Chen S-Y, Lu Z, Goldstein T, Tong J, Chaves A, Kunstmann J, et al. Luminescent emission of excited rydberg excitons from monolayer WSe_2. *Nano Lett* (2019) 19:2464–2471. PMID: 30860854. doi:10.1021/acs.nanolett.9b00029

47. Huang Z, Zhang W, Zhang W. Computational search for two-dimensional $MoSX_2$ semiconductors with possible high electron mobility at room temperature semiconductors with possible high electron mobility at room temperature. *Materials* (2016) 9:716. doi:10.3390/ma9090716